THE ASTROPHYSICAL JOURNAL, 406:12–25, 1993 March 20

THE ADVANCED COSMIC MICROWAVE EXPLORER: A MILLIMETER-WAVE TELESCOPE AND STABILIZED PLATFORM

P. R. MEINHOLD,[1] A. O. CHINGCUANCO,[2] J. O. GUNDERSEN,[1] J. A. SCHUSTER,[1] M. D. SEIFFERT,[1]
P. M. LUBIN,[1] D. MORRIS,[3] AND T. VILLELA[4]

Received 1991 October 25; accepted 1992 August 27

ABSTRACT

We have developed and flown a 1 m diameter Gregorian telescope system for measurements of anisotropy in the Cosmic Background Radiation (CBR). The telescope is incorporated in a balloon-borne stabilized platform with arcminute stabilization capability. To date, the system has flown 4 times and observed from the ground at the South Pole twice. The telescope has used both coherent and incoherent detectors. We describe the development of the telescope, pointing platform, and one of the receivers employed in making measurements of the CBR. Performance of the system during the first flight and operation on the ground at the South Pole are described, and the quality of the South Pole as a millimeter wave observing site is discussed.

Subject headings: cosmic microwave background — large-scale structure of universe — telescopes

1. INTRODUCTION

1.1. *Theoretical Background and Present Status of CBR Anisotropy*

The Cosmic Microwave Background Radiation (hereafter CBR) is generally interpreted as a remnant of the big bang. Compatibility with the known properties of the CBR is a stringent test for any theory of cosmology that attempts to explain the overall dynamics of the universe. The angular distribution of the CBR is a probe of the large-scale structure and dynamics of the universe. There are a number of mechanisms for producing anisotropy in the CBR, and predictions based on very few assumptions make isotropy measurements good tests of standard cosmological models.

Until recently, the dipole anisotropy was the only anisotropy of the CBR to be measured, first reported by Conklin (1969), Corey & Wilkinson (1976), and Smoot, Gorenstein, & Muller (1977), and mapped in detail by Fixen et al. (1983); Lubin, Epstein, & Smoot (1983), Lubin & Villela (1985), the Soviet *RELICT* satellite (Strukov & Skulachev 1984), and recently by Cottingham et al. (1990), Meyer, Page, & Cheng (1991), and the *COBE* satellite (Smoot et al. 1991). The dipole has an amplitude of 3.36 ± 0.1 mK in the direction $l = 264.^{\circ}7 \pm 0.^{\circ}8$, $b = 48.^{\circ}2 \pm 0.^{\circ}5$ (Smoot et al. 1992); heliocentric coordinates). The accepted explanation for the dipole is in terms of a Doppler shift from our motion relative to the frame of the CBR (the "comoving" or Hubble expanding frame), giving a "peculiar velocity" of 370 km s^{-1}, which is the motion of the Sun relative to the CBR. This type of anisotropy is "nonintrinsic," being considered a local effect, rather than one intrinsic to the CBR itself. The *COBE* team has announced a statistically significant detection of anisotropy on a range of scales from 10° to the quadrupole. This measurement is of great importance to theories of large-scale structure and will have a large impact on future searches for anisotropy at all scales.

Recently much work has been done on intermediate scales (angular sizes from 10′ to 10°). The principle mechanism for production of anisotropies in the CBR is the Sachs-Wolfe effect (Sachs & Wolfe 1967). Sachs & Wolfe calculated the gravitational redshifts experienced by a photon traveling from the surface of last scattering. Large-scale fluctuations in the gravitational potential at last scattering red- or blueshift the photons, and local gravitational perturbations red- or blueshift them as they arrive. In the wake of the *COBE* DMR detection, measurements in this range will be of continuing importance in determining the statistics of the fluctuations and the fluctuation spectrum in the small angle range. In particular, studies at these angles might give information about the ionization history of the universe.

At the lower end of this angular range, microphysical processes and structure evolution become important. This angular range is especially relevant for placing constraints on theories of galaxy formation using CBR anisotropy measurements, since these angular scales correspond to the distance scales for clusters of galaxies. Cold dark matter (CDM) models in particular have been investigated in some detail and show peaks in the predicted fluctuation spectrum at these scales (Vittorio, Matarrese, & Luccin 1988; Bond & Efstathiou 1987). Figure 1 is a plot of predicted fluctuation spectra from Bond et al. (1991). Curves of the normalized fluctuation spectrum for CDM, and baryonic isocurvature (BIsoc), for "standard recombination" (SR) and "no recombination" (NR) are shown, as well as calculated sensitivity filters for several recent experiments. The angular range from 10′ to a few degrees is a very good region to test these theories.

Below $\sim 10'$, primordial fluctuations begin to be smoothed due to the finite thickness of the surface of last scattering (Silk 1984). Fluctuations from the Rees-Sciama effect (fluctuations produced by evolving gravitational potentials after decoupling; Rees & Sciama 1968) are not smoothed by this mechanism.

There are other mechanisms for producing CBR anisotropies. Two commonly discussed ones are the Sunyaev-Zel'dovich (SZ) effect and topological effects associated with cosmic strings. The SZ effect is due to inverse Compton scattering of CBR photons off of hot electrons, expected to be found in clusters of galaxies which show X-ray emission from

[1] Department of Physics, University of California, Santa Barbara, CA 93106.
[2] Agrivision Engineering, Inc., Davis, CA 95617.
[3] Morris Research, Inc., Berkeley, CA 94704.
[4] INPE Divisao de Astrofisica, CP 515, 12201 Sao Jose dos Campos, Sao Paulo, Brazil.

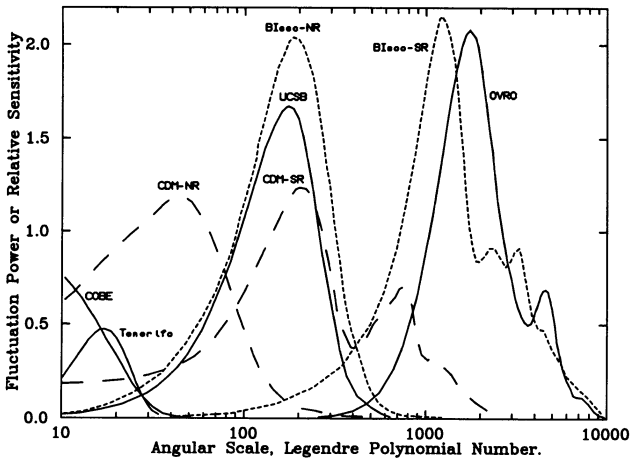

FIG. 1.—Filter functions (*solid curves*) for the South Pole (Meinhold & Lubin) experiment, the OVRO (Readhead et al. 1989) and Tenerife (Davies et al. 1987) experiments, and the *COBE* differential microwave radiometer experiment (Smoot et al. 1990). Normalized angular power spectra (*dashed curves*) for various structure formation theories referenced in the text. The product overlap of a filter function and the angular power spectra can be used to optimize an experiment to test a structure formation theory. (Figure taken from Bond et al. 1991).

hot plasma (Sunyaev & Zel'dovich 1972). The inverse Compton scattering in this case is highly localized in known regions of the sky corresponding to clusters of galaxies believed to contain hot plasma and should produce a clear signal in the CBR. Angular scales for SZ vary with cluster size, but range from several arcseconds up to tens of arcminutes. Strings are able to produce CBR anisotropy two ways: first, they serve as seeds for non-Gaussian structure formation; and second, they have the unique property that the space nearby has the topology of Minkowski space with a slice missing. This results in a net path length difference between the two sides of a string, producing an effective red shift on one side and blueshift on the other. These fluctuations will be very sharp and have highly non-Gaussian statistics. Some predictions suggest very small scale anisotropy on scales of 1′ or less, from highly distorted strings, while others expect linelike discontinuities with linear coherence over degree scales (Bouchet, Bennett, & Stebbins 1990).

Figure 2 shows current limits on CBR fluctuations as a function of angular scale, along with the *COBE* detection. Where possible, the upper limits for Gaussian autocorrelation functions have been plotted

$$C(\alpha, \sigma) = C_0 e^{-(\alpha^2/2\sigma^2)}, \quad (1)$$

Where $C(\alpha, \sigma)$ is an ensemble average over the sky of T_1 T_2, α is the angle between points 1 and 2, σ is referred to as the "angular scale," and $(C_0)^{1/2}$ is the RMS sky fluctuation level. Upper limits on monochromatic models from maps of the background radiation are generally substantially lower than the corresponding limits on Gaussian models. This is a result of the large number of independent determinations of the amplitude of a given sky signal available in a map. For the experiment described below, the monochromatic correlation function upper limit would be a factor 2–3 lower than the Gaussian correlation function upper limit calculated. At small angular scales, however, constraints on monochromatic models are of limited utility, since most realistic models are more closely approximated by randomly distributed Gaussian fluctuations.

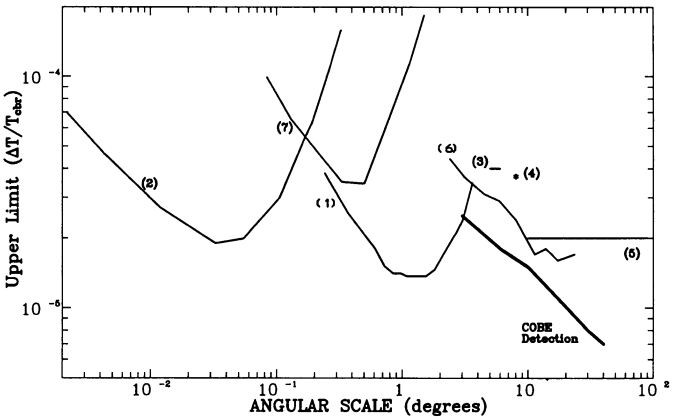

FIG. 2.—Current 95% confidence upper limits on CBR anisotropy with *COBE* DMR detection: (1) Gaier et al. (1992), (2) Readhead et al. (1989), (3) Melchiorri et al. (1981), (4) Davies et al. (1987), (5) Strukov et al. (1984), (6) Meyer, Page, & Cheng (1990), (7) Meinhold & Lubin (1990), (*COBE*) Wright et al. (1992).

1.2. *System Overview*

In 1984 we started development of a telescope for investigating CBR anisotropy at intermediate angular scales. The system was originally designed as a stabilized balloon platform with a 1 m f/1 telescope operating at 3.3 mm wavelength using a Superconductor-Insulator-Superconductor (SIS) receiver, with a full width at half-maximum (FWHM) beam response of 0°.3–0°.8. The system is referred to as the Advanced Cosmic Microwave Explorer (ACME).

The SIS detector was chosen to work at 3.3 mm, near the minimum for Galactic emission as calculated using cosec b^{II} fits to large scale measurements (Lubin et al. 1985), and in an atmospheric window. Figure 3 shows the atmospheric emission at balloon altitude, South Pole altitude, and sea level, calculated from the emission lines for ozone, water, and oxygen, and a standard atmospheric model. The experiment is designed to probe angular scales of interest for galaxy formation theories, with a Gaussian beam of FWHM adjustable from 20″ to 45″, and a mechanism to chop the beam on the sky

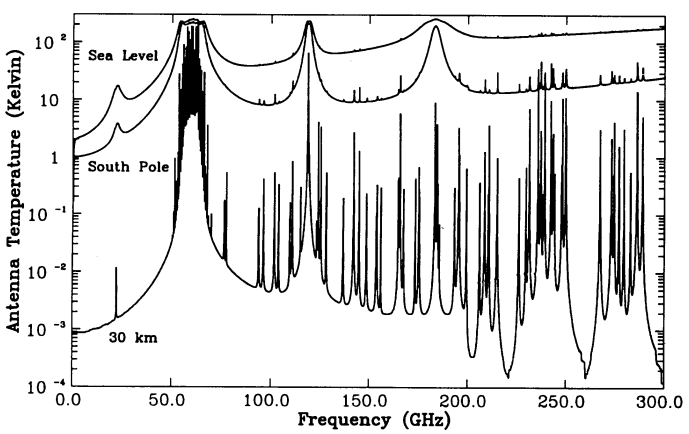

FIG. 3.—Atmospheric emission calculated from JPL Line Catalog and US Standard Atmosphere, for 30 km, 3.6 km (South Pole barometric altitude), and sea level.

by 1° or more. The detector system is a heterodyne receiver, with a bandpass of 550 MHz and a full band receiver noise of 40 K. For this noise temperature and bandwidth, the theoretical integration time to reach a 1 σ error of 1×10^{-5}, or 27 μK, for the temperature difference between two patches is 4.4 hr.

The telescope is designed to operate at an altitude of 30 km, under a stratospheric helium balloon. A good part of the effort on this project involved design, construction and testing of a pointing platform of sufficient stability, accuracy, and flexibility to perform the measurement at this altitude. The pointing requirement is an RMS error of less than 3′ (1/10 of the beam FWHM) in both elevation and azimuth, to avoid smearing of the beam and loss of integration time on target patches of sky.

The system was first flown from Palestine, Texas, in 1988 August using the SIS receiver system. The platform achieved the stabilization requirements for the elevation and did even better for the azimuth control. The system was next taken to the South Pole from 1988 November to 1989 January where measurements of the CBR were done from the ground.

The platform was also flown in 1989 November, in 1990 July, and in 1991 June, using a highly sensitive multichannel bolometric detector, in collaboration with groups at UC Berkeley (the Millimeter Anisotropy eXperiment or "MAX" collaboration, part of the NSF Center for Particle Astrophysics) (Fischer et al. 1992; Alsop et al. 1992; Devlin et al. 1992; Meinhold et al. 1992). This system uses a ^{3}He cooled photometer operating around 3.3, 1.67, 1.11, and 0.83 mm wavelengths, and has a separate secondary mirror, nutation system, calibrator, and associated flight electronics.

From 1990 November to 1991 January the telescope took data from the ground at the South Pole with both the SIS receiver, and an extremely low noise four channel High Electron Mobility Transistor (HEMT) amplifier system operating between 25 and 35 GHz. Table 1 summarizes the measurements made with the telescope to date (note that the system sensitivities quoted are *measured* 1 σ noise in 1 s for $\delta T_{\rm cbr}$ and include chopped atmospheric noise contributions. Data from the 1988 SIS South Pole expedition have been used to put upper limits on Gaussian anisotropies in the CBR at 20″–30″ Gaussian σ and to place constraints on CDM parameters (Meinhold & Lubin 1991; Vittorio et al. 1991; Bond et al. 1991).

This article describes the telescope, stabilization system, SIS receiver, and some of the data taken from the South Pole station in 1988. Details on the bolometric system and data taken with it can be found in Fischer et al. (1992); Alsop et al. (1992); and Meinhold et al. (1992). Data taken on the system using the HEMT detector from 8 to 12 mm are discussed in Gaier et al. (1992).

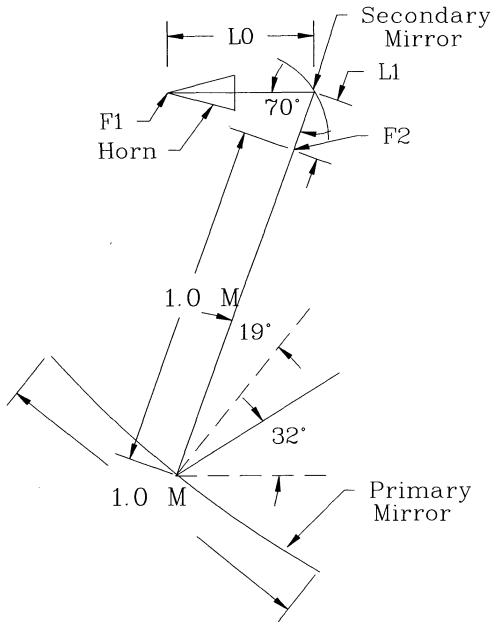

FIG. 4.—Telescope geometry. The aperture of the horn is imaged onto the primary through the secondary. l_0 and l_1 are the distances of the two foci of the ellipsoid from the secondary mirror, l_2 is the focal length of the primary mirror.

2. OPTICAL SYSTEM

2.1. *Design*

The telescope is an off-axis Gregorian design based on work at Bell Telephone Laboratories (Dragone & Ruscio 1985). Figure 4 shows the layout of the horn, secondary reflector, and primary mirror.

The aperture illumination of the horn is a J_0 Bessel function, scaled to have its first zero at the horn wall. Its phase distribution is a spherical wave emanating from the horn apex, which coincides with the first focus of the secondary. The second focus is placed at the focus of the primary. The figure of the secondary mirror is cut so that the aperture of the horn is imaged onto the primary mirror, as derived from the lens equation

$$\frac{1}{f_1} = \frac{1}{t_0} + \frac{1}{t}, \tag{2}$$

where t_0 is the distance from the horn aperture to the secondary, $t = l_1 + l_2$ is the distance from the secondary to the primary, and f_1 is the focal length of the secondary mirror, defined by

$$\frac{1}{f_1} = \frac{1}{l_0} + \frac{1}{l_1}. \tag{3}$$

TABLE 1

CBR MEASUREMENTS WITH THE UCSB PLATFORM

Date	Site	Detector System	Beam FWHM	Sensitivity
1988 Sep	Balloon (Palestine, TX)	90 GHz SIS receiver	0°.5	6.5 mK $s^{1/2}$
1988 Nov–1989 Jan	South Pole	90 GHz SIS receiver	0.5	6.1
1989 Nov	Balloon (Fort Sumner, NM)	MAX photometer (3, 6, 9, 12 cm^{-1})	0.5	12, 2, 5.7, 7.1
1990 Jul	Balloon (Palestine, TX)	MAX photometer (6, 9, 12 cm^{-1})	0.5	0.7, 0.7, 5.4
1990 Nov–1990 Dec	South Pole	90 GHz SIS receiver	0.5	6.1
1990 Dec–1991 Jan	South Pole	4 Channel HEMT amp (25–35 GHz)	1.5	0.8
1991 Jun	Balloon (Palestine, TX)	MAX photometer (6, 9, 12 cm^{-1})	0.5	0.6, 0.6, 4.6

l_0 and l_1 are the two focal lengths of the elliptical secondary, and l_2 is the focal length of the primary mirror. These constraints insure that the telescope is focused, because the image of the aperture is now a spherical wave diverging from the focus of the primary (Thomas 1978). The primary illumination is approximately given by the magnified image of the horn aperture, with the magnification given by t/t_0. Since the illumination of the primary mirror is just the magnified image of the aperture distribution of the horn, the telescope has excellent efficiency and sidelobe performance, similar to that of the scalar feed horn.

The scalar feed horn is 12.5 cm long, with a 4.4 cm diameter aperture, giving a (FWHM) of 6°.5. The secondary has $l_0 =$ 29.1 cm, $l_1 = 15.9$ cm, and thus $f_1 = 10.3$ cm. The aperture of the horn is $t_0 = 11.3$ cm from the secondary, and using equation (2), the magnification is $t/t_0 = (l_1 + l_2)/11.3$ or 10.3. This implies a primary illumination diameter of 45.8 cm, showing how underilluminated the primary is. The main lobe response of the telescope in the far field can be approximated using Gaussian beam optics. The beam profile can be parameterized by the beam radius "ω," with the electric field given by

$$E = E_0 e^{-\rho^2/\omega(z)^2} \tag{4}$$

with

$$\omega(z) = \omega_0 \sqrt{1 + \left(\frac{\lambda z}{\pi \omega_0^2}\right)^2}, \tag{5}$$

where z is the distance along the beam direction from the beam waist, ρ is a distance perpendicular to the beam axis, and ω_0 is the beam "waist," the minimum radius. For conical scalar feed horns of the type used, the beam radius at the aperture can be approximated by $a \times 0.64$, where a is the aperture radius. This is the best-fit Gaussian to the Bessel function. As discussed above, the magnification is 10.3, so the magnified image of the beam radius appearing on the primary is 14.5 cm. Since the parabola changes the phase distribution of the beam from spherical to flat, this is the waist of the beam of the telescope. For large z, equation (5) gives the FWHM of the beam as FWHM $= 2 \arctan (0.5887\lambda/\pi\omega_0)$, or 0°.5. Three different secondaries of varying magnification were made, which can be used with the same primary to give beams of 20′, 30′, and 50′ FWHM at 3.3 mm wavelength. In addition, other secondaries have been used for the HEMT and bolometric detectors.

2.2. *Construction*

The primary mirror is a 1 m diameter section of a paraboloid of revolution, and it has an effective focal length of 1 m. It was machined on a numerically controlled mill out of a single piece of cast aluminum (MIC-6) at Bell Laboratories, under the direction of P. Moyer and J. Stack. The machining process was designed to keep the surface accuracy and roughness better than 0.05 millimeters or $\sim$1/50th of a wavelength. This is small enough that effects on the main lobe are small compared to the diffraction limit from the finite aperture size, although the effects on the far sidelobes are difficult to quantify.

In addition to the primary, three secondaries were made, to produce the primary beam FWHMs of 20′, 30′, and 50′ mentioned above. The beam sizes were chosen so that for every secondary, the primary is highly underilluminated in order to reduce chopped spillover and edge diffraction.

The basic requirements of the telescope optics allowed some freedom to choose the orientation of the different elements. The detector is mounted in a "side-looking" dewar, and the primary mirror is at the lowest point. Rejection of direct paths of radiation into the horn is accomplished by a combination of the primary baffles and a separate set of baffles around the secondary. In order to chop the beam on the sky, the secondary mirror is nutated about the axis of the horn, thereby changing the position of the image of the aperture on the primary.

Rotation of the secondary through an angle α moves the image of the horn apex by a distance $l_1 \sin \beta \tan \alpha$ in the focal plane of the primary, where $\beta = 70°$ is the angle between the incident and reflected beams off the secondary. Simple ray tracing shows that the primary beam on the sky will then be moved by an angle Θ given by $\Theta = \arctan [(l_1/l_2) \sin \beta \tan \alpha]$, so a rotation of 6°.6 corresponds to a motion of 1° on the sky. If the beam is thrown through an angle of $\pm$0°.5 then the spot on the primary moves 6.3 cm away from the center.

Using the spot radius on the primary mirror of 14.5 cm calculated above, a rough estimate of the spillover at the edge of the 1 m dish can be calculated: the center of the spot is 43.7 cm from the edge, so equation (4) gives a field strength at the edge of 1.1×10^{-4}, corresponding to a power level of -78 dB relative to the center. This is only an estimate using the Gaussian beam approximation, the actual illumination is almost certainly higher. Direct measurements of the primary illumination are extremely difficult to do reliably at such low levels, due to standing wave problems with coherent sources, and near field and illumination problems associated with the feeds used as test sources. The telescope optics has been tested by measuring beam patterns and calibrations in the far field.

2.3. *Testing*

The telescope response was measured in three different ways: on an antenna range behind the physics building at UC Santa Barbara; using Jupiter as a thermal point source during the first flight; and using the Moon as a thermal source, calculating the emissivity over the surface for the proper lunar phase and wavelength at the South Pole.

For the test range measurements, the source was a Gunn diode operating at 90 GHz, with output power of 10 mW, coupled to a scalar feed identical to the one used as the feed-horn in the telescope. The source was situated on top of the physics building at a height of 20 m, 45 m from the telescope. Scanning of the beam was accomplished using the elevation portion of the stabilized platform altitude-azimuth mount (see Fig. 8, below). The detector used for the UCSB beam tests was a heterodyne receiver similar to the flight system, but using a Schottky diode mixer at ambient temperature. A dynamic range of 85 dB was obtained by a combination of attenuation at the source, attenuation in the IF section of the detector, and, for the lowest power levels, chopping the source at 1 kHz and using a lockin amplifier. The 85 dB limit is set by the signal-to-noise and stability of the source/detector combination. In addition, the test range is probably not adequate for measurements much below this level due to the possibility of spurious response from nearby objects such as buildings and trees.

The three primary questions to be answered about the telescope response are (1) What is the main lobe response, particularly FWHM and forward gain? (2) Is the far sidelobe response level acceptable for the projected thermal signal-to-noise of the measurement, and how is this affected by various baffling schemes? (3) What effect does moving the beam on the sky by rotating the secondary have on the beam pattern?

Figure 5 shows two measurements of the main lobe of the

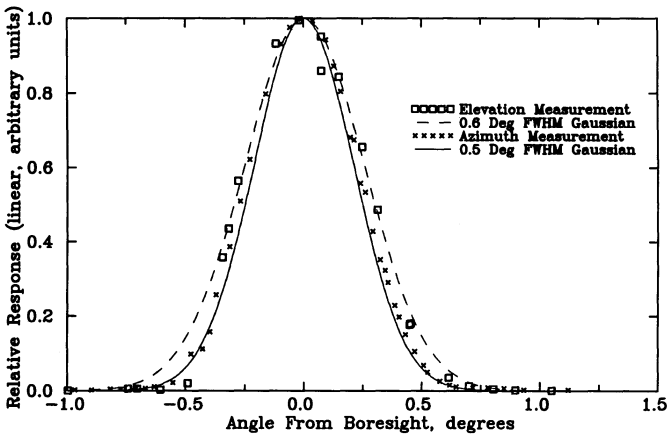

FIG. 5.—Antenna main lobe measurement in elevation (*open boxes*) and in azimuth (*crosses*), with Gaussians of FWHM = 0°.6 (*dashed line*) and FWHM = 0.5 deg (*solid line*).

antenna performed on the test range, along with two Gaussians. The FWHM of the telescope using this secondary is predicted to be 0°.5. Both the azimuth and elevation measurements are best fit by a FWHM of 0°.6. Figure 6 which shows a scan of Jupiter from the 1988 August flight, along with the response expected from a point source from a 0°.5 FWHM beam (solid line). Note that part of the left side of the scan (the negative beam side) is contaminated by elevation pointing errors, causing the negative peak to look rough, and smaller than the right one.

Figure 7 is a plot of the antenna response out to the noise floor of 85 dB. No structure appears at angles greater than ~35°. Measurements were made to this sensitivity for many test configurations: for two of the three secondary mirrors; with a small aperture baffle placed between the secondary and the primary mirrors close to the waist; for slight changes in positions of the dewar and secondary; with microwave absorbing material placed at possible stray reflection points, etc. In all cases, the basic response was consistent with the one shown: the main lobe was slightly wider than calculated, and the sidelobe response was acceptable, but above that predicted by calculations. Both of these effects can be attributed to the near

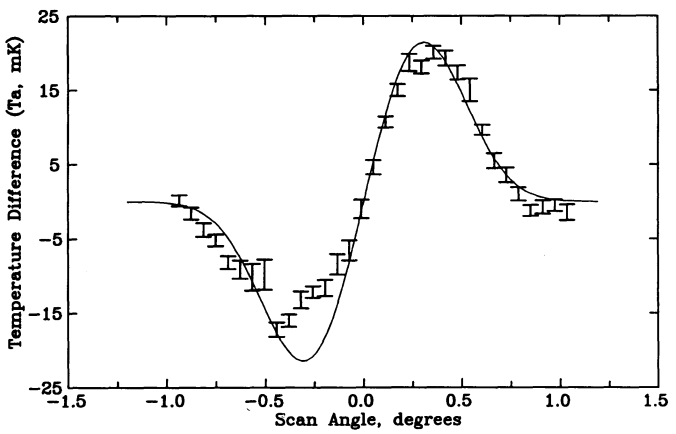

FIG. 6.—Jupiter scan from 1988 August SIS balloon flight (*error bars*), with calculated point source response using FWHM = 0°.5 (*solid line*). Note that elevation pointing instability caused the negative chopped beam response to be uneven and smaller than the positive beam.

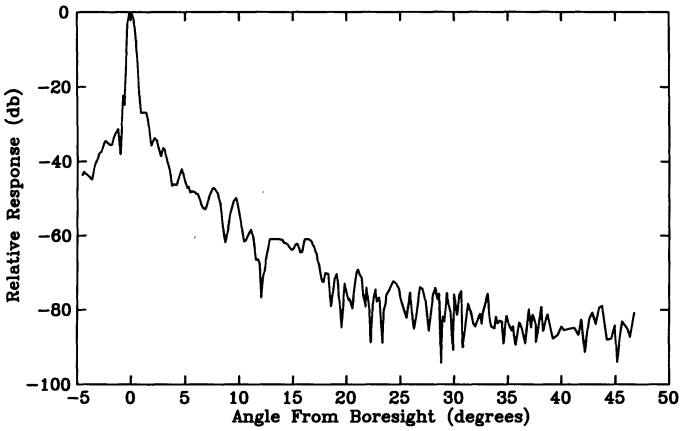

FIG. 7.—Measured antenna response out to noise floor of 85 dB

field measurement, although some of the excess far sidelobe response could be due to defocusing or surface irregularities. Low sidelobe measurement scans in azimuth could not be done on the test range due to the large number of buildings and trees giving spurious reflections, the effects of which are minimized in the elevation scan measurements. In addition to the tests above, complete sidelobe and main lobe measurements to the noise limit were performed with the secondary mirror fixed at the extremes of the rotation used in the CBR measurements, in order to look for defocusing and spillover effects. There were no significant changes seen.

The beam efficiency of the telescope is an important number to know for calibrations and for setting upper limits. In this case, the relevant number is the ratio of integrated power in a Gaussian beam with FWHM of 0°.5 to the total integrated power in the actual beam response. This is a difficult comparison in this case since the measured beam pattern includes the above mentioned near field measurement effects, and a full two-dimensional beam map to the noise floor does not exist. The real efficiency may be approximated by fitting the main lobe of Figure 7 to a Gaussian, and comparing the integral of that Gaussian to a numerical integration of Figure 7. The result of this is 99% efficiency. Integrating just the main lobe data (0°–1°) directly and comparing to the entire pattern integrated power gives 95% efficiency, which could be used in setting upper limits in order to be conservative. The measurements of the beam response discussed above are not full two-dimensional maps, so there may be distortions of the main lobe which are not apparent in these tests. The main concern is not that the beam be exactly a two-dimensional Gaussian, but that the effective efficiency be high. As a cross check of the near field measurements, calibrations performed at the South Pole using the Moon help to confirm the general numbers for beam efficiency. The Moon measurement has errors of order 10% and is described in § 5.4.

2.4. *Beam Nutation System*

As noted above, the chop is accomplished by nutating the secondary mirror about the axis of the feed horn. The mechanism which does the nutation is a resonant system, driven by a DC servo motor with an absolute angle encoder attached to the mirror shaft. The mirror is directly coupled to the motor shaft, and the shaft is connected to the motor housing and a counterweight via several springs, chosen to make the system resonant at 8 Hz. The driving circuit is a hardware servo,

which maintains the frequency of oscillation at 8 Hz, and the amplitude constant to less than 1%. The zero position of the mirror is set by two weak centering springs which couple the motor housing to the telescope frame. Running the nutation in this way has the major advantages of low power consumption (~20 watts) and very low vibration: since the motor housing and counterweight rotate opposite the mirror, very little vibrational energy is transmitted to the frame of the telescope at the turning points. This mechanism operated reliably during the first flight and during most of the data taking at the South Pole. For subsequent expeditions, different resonant nutation systems have been used, employing torsion fibers instead of springs, with higher stability and reliability.

3. POINTING AND STABILIZATION SYSTEMS

3.1. *Summary*

The original goal to fly the telescope at 30 km required development of a stabilized pointing platform for operation in the balloon environment. With some modest additions, the system was also able to do measurements from the ground at the South Pole. The stabilization systems, design, software, testing, etc., were primarily the thesis work of one of us, A. C. (Chingcuanco 1989; Chingcuanco et al. 1990).

3.2. *Balloon Platform*

A schematic drawing of the gondola is shown in Figure 8. The platform is suspended from a 0.1–1.0 million m^3 balloon by the parachute and a 20 m steel cable "ladder." The system is an az-el mount, the aximuth motion accomplished by moving the entire frame, and elevation by moving the inner frame, to which the telescope is mounted. The requirement is to remove motions associated with the balloon, to point at target positions, and to track these positions over time while maintaining better than 3′ rms stability. There are three major parts to the servo control and data acquisition system: the attitude sensor elements; the attitude servo mechanisms; and the computer, software, and telemetry control system.

The primary attitude sensing element is the Attitude Reference Unit (ARU). The ARU uses a self-contained three-axis gyro and accelerometer with a navigation processor, capable of absolute attitude sensing and readout to 20″. The ARU is comounted with the telescope and interfaced to the flight computer. The ARU gives angles to a fraction of an arcminute but can have drifts of up to $1° \text{ hr}^{-1}$, depending on its velocity and acceleration. As an absolute check on the pointing, a CCD camera with a 135 mm focal length lens and a $2° \times 3°$ (elevation time azimuth) field of view is coaligned with the telescope beam. The image from this camera is telemetered down over a National Scientific Balloon Facility (NSBF) transmitter and is used during flight to confirm the absolute pointing on fiducial stars and to correct for ARU drift. A three-axis magnetometer is used as a secondary azimuthal sensing element in case of ARU failure and for realigning the gyro at float altitude. The secondary sensing element for the elevation was a capacitive bubble level for the first flight and a 16 bit analog shaft encoder for the other flights. This gives arcminute resolution of the position of the telescope relative to the gondola frame. A second CCD star camera has been implemented for later flights. This camera incorporates an image intensifier and a motorized zoom, allowing star tracking to around 10th magnitude, and the increased flexibility of a variable field of view.

The three principle servo mechanisms are a decoupling mechanism which isolates the package from the balloon, dumps angular momentum to the balloon and performs coarse azimuth positioning; a flywheel for fine azimuth control; and a ball screw linear actuator with either a hardware servo or a microstepped stepper motor for elevation control of the inner frame.

Since the balloon is ~50–100 m in diameter it is likely to be subject to wind shear, causing random rotations. For this reason the azimuthal motions of the payload are decoupled from the balloon by means of an active triple race bearing system (the "R^3"). The R^3 has two motors which are used in three ways. First, in normal operation, the races of the bearings

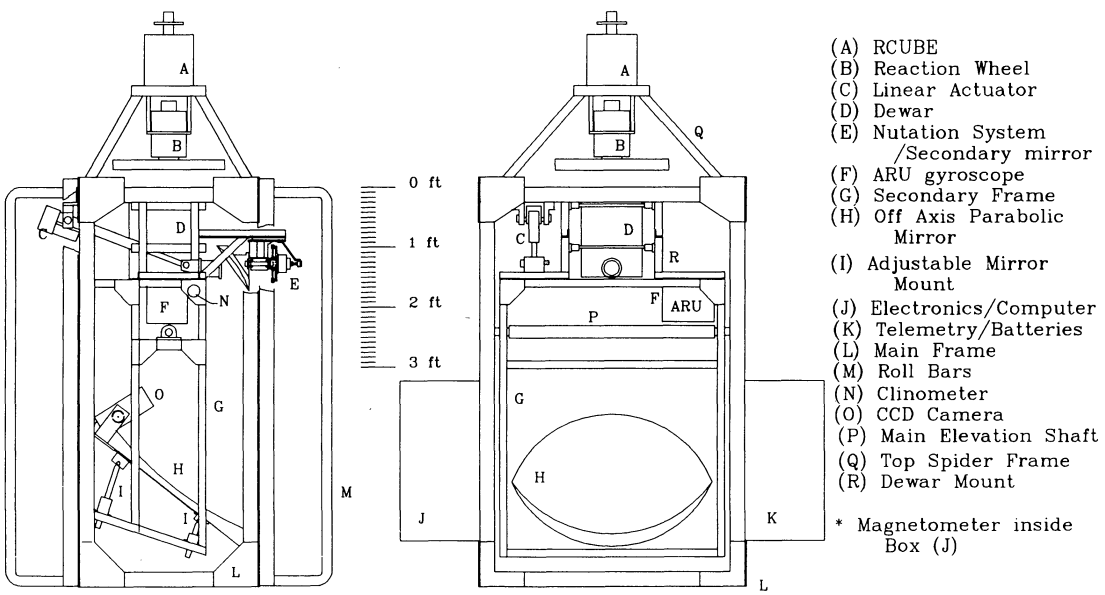

FIG. 8.—Scale drawing of gondola, including all major servo hardware and telescope elements

are kept moving by the small gear motor to reduce friction. Second, when the flywheel rotation rate gets too high, the R^3 can drive the gondola directly against the flight line to dump angular momentum to the balloon. Third, when the desired azimuth is far from the current one, the R^3 motor is used to turn the package until it is close enough to use the flywheel.

Fine azimuth control is done with a large flywheel/torque motor combination, controlled by the flight computer with a Proportional, Integral, Differential (PID) control algorithm. The flywheel is a 58 cm diameter aluminum disk with a moment of inertia of 0.94 kg m^2 and is driven by two 2.7 Nm torque motors. A tachometer is attached to the shaft to monitor the flywheel velocity and the output is used by the servo code to determine how much balancing torque to apply at the R^3. The interaction between the parts of the system is shown schematically in Figure 9. In addition to the PID control algorithm, a model referenced adaptive control algorithm was implemented which adapts its control parameters based on actual system response (Chingcuanco 1989). This control method is more stable to perturbations and changes in system parameters, but does not perform as well as the PID algorithm during normal conditions.

The flight computer is an 80186 CPU-based system, with STSD and SCSI bus interfaces for the data acquisition hardware. During flight, a servo code runs on the flight computer, taking data on the attitude and calculating appropriate error signals using PID or model referenced adaptive control (refer to Chingcuanco 1989 for details). In addition, housekeeping data and science data are recorded on disk and telemetered to the ground. Changes in the operation of the servo, such as target changes, position updates, drift offsets, etc., are accomplished by command uplink to the servo code through a 408/416 MHz full duplex telemetry system. When the servo code is not running, the flight computer can be operated from the ground through the telemetry system as a remote terminal at 4800 baud.

Figures 10 and 11 show the overall performance of the system for the second flight (1989 November). Figure 10 is the azimuth relative to a fiducial tracking point during a deep integration on a potential Sunyaev-Zel'dovitch source, using a three-position scan strategy. After slewing and settling time, the rms error in azimuth is less than 1. The fraction of time spent within 1.″5 of the three measurement positions is 91%. For other flights a smooth scan strategy has been implemented which improves the scan rate and efficiency. A benchmark test was performed during this flight, tracking a point of constant α, δ, with no scanning. The azimuth and elevation error are shown in Figure 11. A periodic motion in elevation of $\sim$1.′5 amplitude and 15 s period is evident in Figure 11. This appeared throughout the flight, decreasing at later times, and is due to pendulation of the entire gondola from either the point where the flight train connects to the balloon, or the center of lift of the balloon. Since the flight train is $\sim$50 m long, the period is $\tau = 14$ s, consistent with the measurement. The data shown above have an rms azimuth error of $\sim$0.″4 and an rms elevation error of 0.″9, both well within the original design goals.

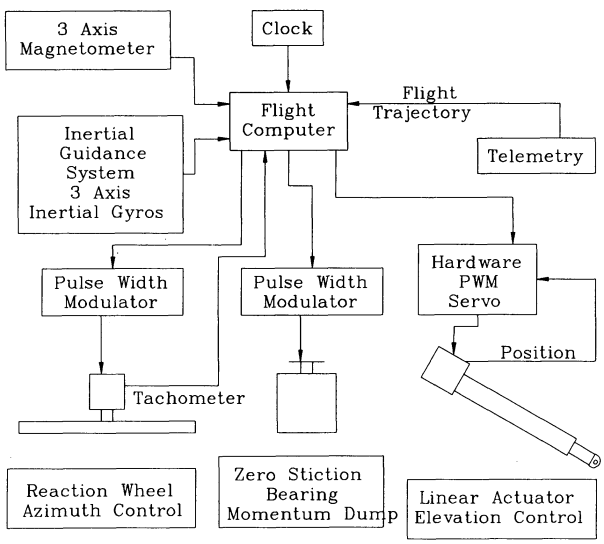

FIG. 9.—Diagram of the interaction between all portions of the servo system.

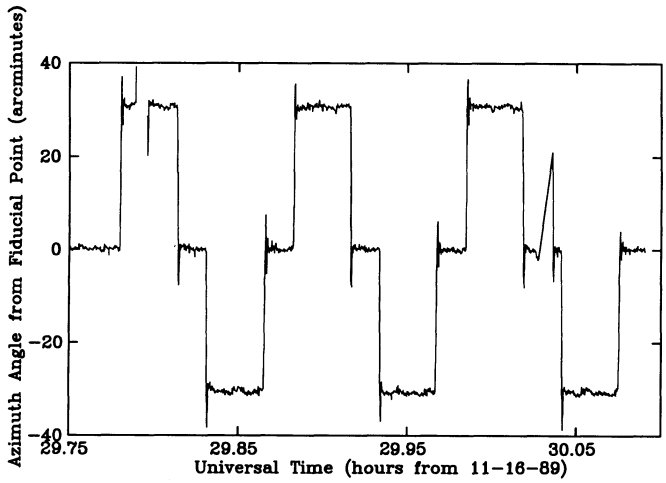

FIG. 10.—Azimuth pointing performance from the second flight (1989 Nov 16). Azimuth angle as a function of time is shown for a three-position scanning strategy. The pointing error within a given azimuth bin is smaller than 1′.

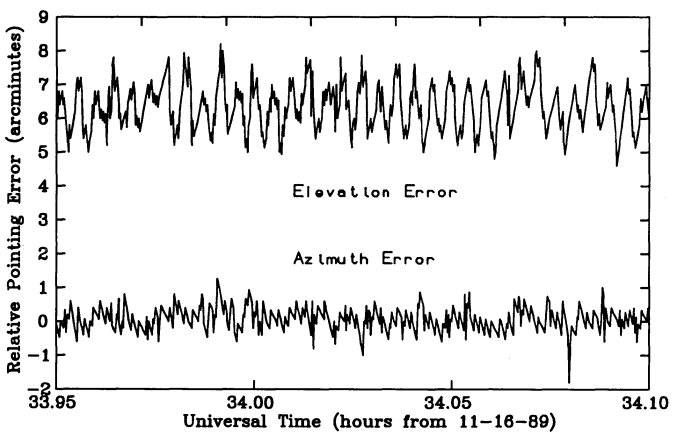

FIG. 11.—Pointing performance from the second flight (1989 Nov 16). Azimuth and elevation angle errors as a function of time are shown for tracking a fixed right ascension and declination. The elevation error displays a 1.′5 peak to peak pendulation of the payload.

3.3. *Ground-based System: South Pole Trips*

For observations at the South Pole, the azimuthal control portion of the gondola is replaced with a large rotation table. The elevation control and data acquisition operate as in flight. The ARU gyros do not work well at high latitudes, so an analog angle resolver mounted to the fixed rotation stage frame was used to measure azimuth to 16 bits (20″). The elevation was kept fixed for the primary data taking and was checked with external inclinometer.

The tracking rotation table consists of a flat top and a large aluminum cone, which is driven directly by two large stepper motors, resulting in a system with essentially no backlash. The stepper motors are driven with 25,000 stepper revolution microsteppers, for increased resolution and smoother operation. The table worked very well for the entire data-taking period, except for a slight problem with efficiency during the 1988–1989 season. With the setup used for that campaign, the stepper motors were unable to start and stop the entire telescope rapidly, and nearly 35% of the time was spent slewing from one position to another. The slewing time for the 1990–1991 season was 10%. The rms error for each field was ~0.′5 in azimuth, corresponding to 0.′14 on the sky. The absolute position was calibrated using the Sun and the Moon. The Moon was visible at the very beginning of data taking, and again at the very end, verifying that the absolute pointing changed by less than 13″ in azimuth, or 3.′6 in actual sky position. This includes all sources of tracking error and may be dominated by the long-term precision of the computer's clock. The system clock was synchronized to UT regularly enough to avoid errors larger than a few arcminutes. As a check on the resolver stability, the position was measured for ~8 hr with the telescope fixed, and the resolver output did not change apart from bit noise. Operating from the South Pole, where tracking requires only azimuth tracking at constant elevation, provides two advantages. First, the elevation tracking requirements reduce to having a stable mounting arrangement and a reasonably accurate number for absolute elevation. Second, since the atmospheric emission measured from the ground is significant, any elevation tracking would induce atmospheric offsets. In addition, any elevation change is a potential source of variable sidelobe pickup.

4. THE RECEIVER

4.1. *Summary*

A schematic of the detector is shown in Figure 12. The entire front end is cooled by liquid helium and consists of a feed horn, a thin-walled stainless steel section as a thermal break, a circular to rectangular waveguide transition, a Bethe hole coupler for local oscillator (LO) injection, and the SIS mixer block. In front of the horn there is a resonant 1.7 mm thick Z-cut quartz window, which is thermally sunk to the 77 K LN_2 surface and acts as an infrared blocking filter, reducing the thermal load on the horn and liquid helium plate. With this infrared blocking window in place, the hold time for helium is ~18 hr, without it is ~4 hr. The thickness of the blocking filter was chosen at a minimum of reflection at 90 GHz, corresponding to one full wavelength in the quartz ($n = 1.95$). Minimum reflection is desirable in this system both to reduce input attenuation and to reduce the amount of LO power which is reflected back into the SIS junction from the window (large amounts of reflected LO power can result in slow variations in gain and sensitivity). In front of the quartz window is a 0.13 mm Mylar vacuum

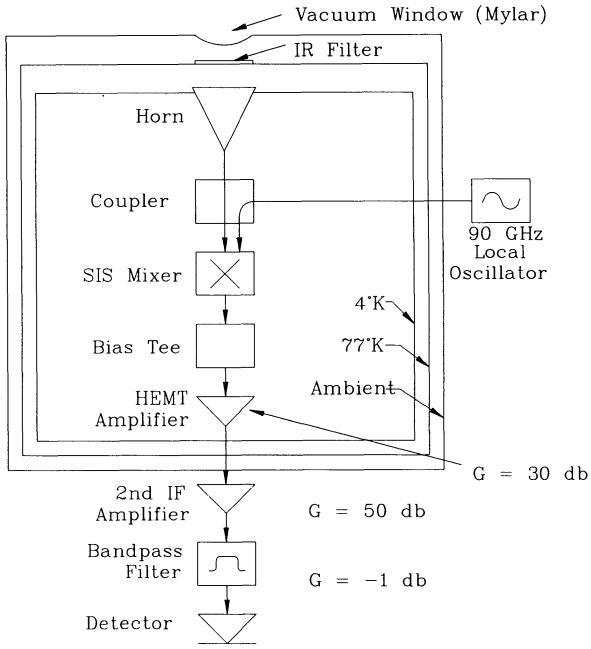

FIG. 12.—Schematic of the SIS receiver system

window. The quartz and Mylar window emission add minimally to the total system noise. After the mixer is a bias tee for putting a DC voltage across the junction and matching the IF output into the High Electron Mobility Transistor (HEMT) amplifier. After this first amplification, the signal is brought out to an ambient temperature amplifier. A coaxial filter is used to define the bandwidth and then the output is sent into a crystal diode detector, giving an output proportional to the incident power, of order 1 mV at the diode per 10^{-13} W input to the horn (the input power from the CBR into the receiver sidebands is $\sim 1.5 \times 10^{-14}$ W).

4.2. *SIS Mixer*

The SIS mixer is a niobium/aluminum-aluminum oxide/niobium junction from the Hypres corporation, mounted in an NRAO mixer block, provided by A. Kerr (NRAO). This is a two backshort block, one for matching the junction to the waveguide input, the other for matching to the IF output port. See Pan et al. (1989) for details on the mixer design. Each backshort is moved by a differential screw mechanism driven by a DC motor operating at liquid helium temperature in vacuum. The initial design of the receiver incorporated a different SIS mixer block. This was a single backshort mixer block, in which the IF matching is accomplished via a stripline structure evaporated directly onto the same substrate which holds the junction. The SIS junctions were a Pb-In-Au alloy. Many of these junctions were tested, but it was found that they were not robust in terms of cycling, UV exposure, or humidity. Niobium is a much more desirable material, both for stability, and its high superconducting transition temperature ($T_c = 9.5$ K), which makes the I–V curve sharper.

The biasing scheme is a four-wire constant voltage circuit, with a 50 ohm resistor in the bias tee in series with the SIS junction and one in parallel with it to protect the junction. By scanning the bias voltage and looking at the output power from the IF system, the photon conversion peaks for the array of junctions can be found. The peaks occur at bias voltages

where one, two, or three photons are enough to assist the quasiparticles across the barrier. The voltage difference between adjacent peaks is 1.48 mV, corresponding to $4 \times 0.37 \times 10^{-3}$ eV, or one 90 GHz photon per junction. The Gunn power level and backshort positions are tuned to maximize conversion for a given photon peak, then the bias voltage is fixed at that peak to operate. System performance is optimized by finding the peak with the lowest noise figure. In general, maximizing the conversion gives the lowest noise, suggesting, along with other evidence, that the system noise is dominated by conversion loss in the mixer and loss in the RF sections.

4.3. *IF System*

The primary improvement of the IF system over previous receivers is the use of a cooled HEMT amplifier with 2 K spot noise for the first stage. The HEMT's we used work best when light is shone on them, so a GaAs LED is mounted to the case of the amplifier to illuminate the HEMT. This HEMT with LED was used during data taking at the South Pole, while an earlier version without LED was used in the flight, the latter having a spot noise around 4 K. The reduction in IF noise achieved with the LED led to a 15 K reduction in overall system noise, again suggesting thast the system limitations are from front end and conversion losses, and possibly IF matching.

After the ~30 dB gain of the HEMT amplifier, the signal is brought out to a second IF amplifier with 50 dB of gain, then through a six pole Chebychev filter and onto a crystal diode detector. The overall system performance is shown in Figure 13, for a mixer physical temperature of 3.5 and 4.7 K. Operating at the South Pole, with slightly lower temperature due to the low ambient pressure (~520 torr) and the full bandwidth of 0.55 GHz, the system had a noise temperature of $T_{sys} = 40$ K. With a pumped liquid helium bath, the receiver had a minimum spot noise of 33 K, making it the lowest noise broadband 3 mm receiver produced at that time. Using the radiometer equation $\delta T = T_{sys}/(\beta\tau)^{1/2}$, where δT is the 1 σ error for bandwidth β in an integration time τ; this system gives 1.7 mK s^{-1}. As the measurement involves chopping between two positions on the sky and integrating the difference, the sensitivity on the sky is 3.4 mk $s^{1/2}$, with modifications to account for the chopping strategy.

5. THE SOUTH POLE

5.1. *Summary*

After the first flight, the system was transported to the South Pole. Operations went smoothly, due to the planning and enthusiastic support of the South Pole station summer staff, who provided working areas, electrical power and other needed help at the Pole, as well as entertainment. In addition, logistical support of the Navy's Antarctic "Deep Freeze" force included transportation of scientists and equipment, as well as a 12,000 liter liquid helium dewar from the US to the South Pole via ski-equipped C-130 military transport aircraft. The system was shipped to Antarctica in late October of 1988. We arrived at the Amundsen-Scott South Pole station in the last week of November and had the system fully operational by the second week of December.

Two principle features of the South Pole Station determine working conditions there during Antarctic summer, constant daylight and stable, very low temperatures. Average temperatures at pole were −40 F in late November, rising to about −25 F by mid-January. NSF polar programs selected Antarctic summer, 1988–1989, to concentrate on CBR anisotropy measurements, with three groups operating a total of five separate instruments, on a variety of angular scales and at different wavelengths. All three groups operated at a site 1 mile from the main station.

The primary reason for making measurements from the South Pole is the atmosphere. Figure 14 shows the precipitable water content at the pole during the 1988–1989 and 1990–1991 Austral summers, calculated by integrating data taken by the South Pole meteorology group using balloon-borne hygrometers. The results should be considered tentative due to hygrometer calibration and stability uncertainties. For comparison, the precipitable water at balloon altitude is 3×10^{-4} mm, and a good infrared observing site like Mauna Kea has 1 mm on good days, so the South Pole is probably the best currently usable ground-based site for this type of work. In addition to the low water content, previous groups reported exceptional stability of the atmosphere at pole (Dragovan 1987), another requirement for the measurement. A discussion of the atmospheric stability information is included below in the section on the data. Figure 15 shows model calculations for the antenna temperature at the South Pole (using the same code as

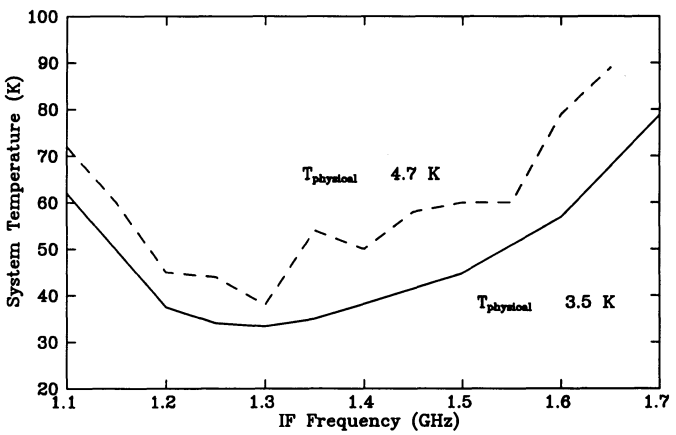

FIG. 13.—Measured total receiver noise temperature in 0.01 GHz bandwidths. IF bandpass is 1.0–1.55 GHz.

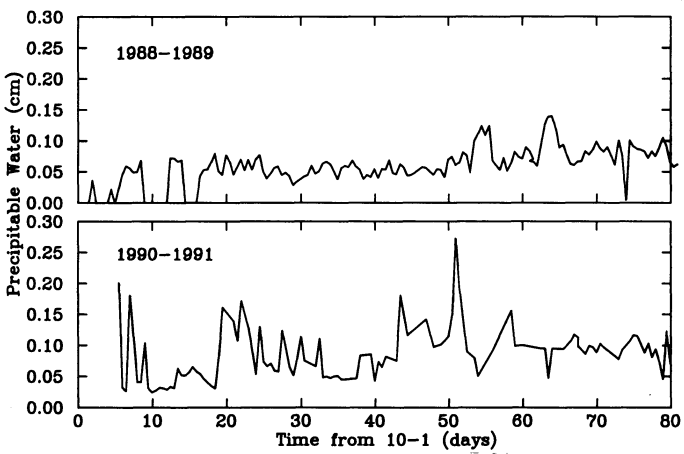

FIG. 14.—Measured precipitable water at the South Pole for 1988–1989 and 1990–1991 austral summers.

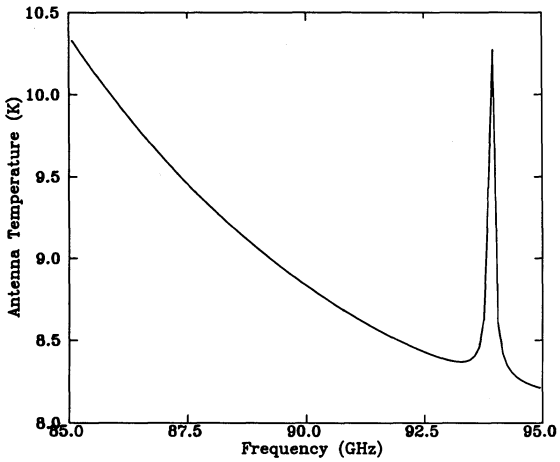

FIG. 15.—Calculated zenith sky temperature for South Pole barometric altitude (3.6 km), not including CBR.

Fig. 3). Figure 16 is the data from a zenith scan, fit to cosecant elevation, giving a zenith sky temperature of 9 K, in reasonable agreement with the model. The same model gives an estimate of the atmospheric opacity at 90 GHz. For the measurement elevation of 73°, there is an effective absorption of ~3.6%.

5.2. *Alignment and Calibrations*

The lack of visible stars during the polar summer presents a problem for telescope alignment. The Sun and Moon were used for this alignment, calculating their positions, and finding them with the telescope beam. When tracking the Sun, the large amount of thermal power made it necessary to cover the mirror with foam to keep the infrared radiation from damaging the system and to intentionally point at a slightly different elevation in order to avoid saturation of the detector. The Moon became available for observation near the beginning and near the end of the measurement time, providing a long-term check on the absolute pointing consistency and an independent calibration. The telescope was maintained at a constant elevation during the deep integrations, even when transferring liquid helium, reducing pointing error to the reproducibility of the azimuth encoder. As described in § 3.3, the servo system azimuth error was small.

Calibrations were performed roughly once per day, by measuring the DC output of the detector (i.e., before the lockin amplifier) when viewing blank sky and when viewing an ambient absorbing target (Emerson Cumings Eccosorb "CV"). Given the telescope elevation and the sky temperature from Figure 16 as well as the temperature of the absorbing target, the calibration constant in mK per volt, and the noise temperature in kelvins can be calculated. Figure 17 shows a scan of the Moon from 1988 December 12 and a calculation of the expected response. The calculation relies on a model of the lunar emission from S. Keihm (JPL), which includes information on the phase of the Moon, its distance, and the measured thermal and microwave properties of the lunar surface. The calculation shown includes the sine wave chop.

5.3. *Measurement Strategy*

As the overall goal was to measure CBR anisotropy at levels of order 10^{-5} of the temperature of the CBR, effective use of integration time and careful control of systematic factors were crucial. Figure 18 shows the arrangement of the measured points. The data essentially consists of a small linear map, measuring the nine temperature differences between 10 30′ patches separated by 1°. The system integrated for ~1 minute per point before moving to the next position, scanning from one side of the strip to the other in a period of ~12 minutes. Having all points adjacent provides a way to check for certain systematic effects, from the atmosphere, from far sidelobe pickup of the Sun, etc. Scanning in both directions makes it possible to distinguishing between time varying offsets and those which change in angle. This is not possible with drift scanning techniques. In addition, by measuring overlapping temperature differences, the data are sensitive to a range of angular scales, from below the beam size of 13′ (σ) up to ~5°. Nine points were chosen since fewer points would make statistics and systematic checks more difficult, while more points would dilute the integration time. The integration time per point was determined by the servo capabilities: the shorter the timescale, the smaller the effects of atmospheric 1/f noise, while the time the servo spent slewing between positions reduced the efficiency for short integration times. The deep integrations discussed below were done with 1 minute intervals between slews, with 2 minutes at the endpoints of the scan to make the

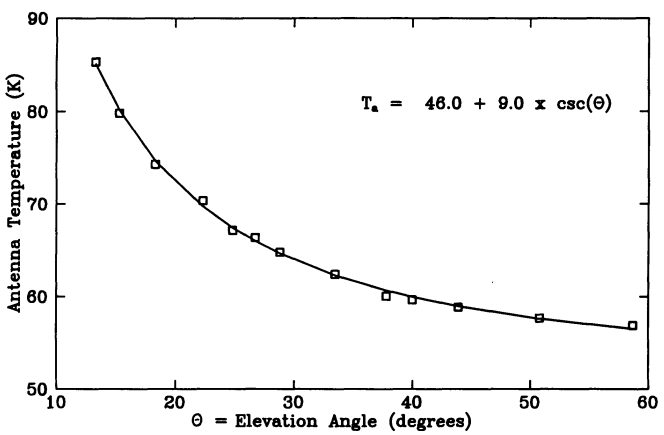

FIG. 16.—Measured antenna temperature as a function of elevation angle at the South Pole on 1988 December 5. The best fit csc (elevation) curve gives a zenith sky temperature of 9 K.

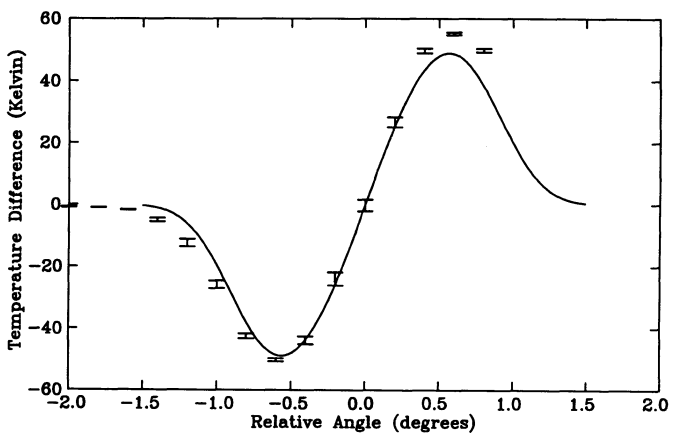

FIG. 17.—Measured Moon scan from the South Pole on 1988 January 12 (error bars) and calculated response (*solid line*) using a lunar regolith model and a sinusoidal chop.

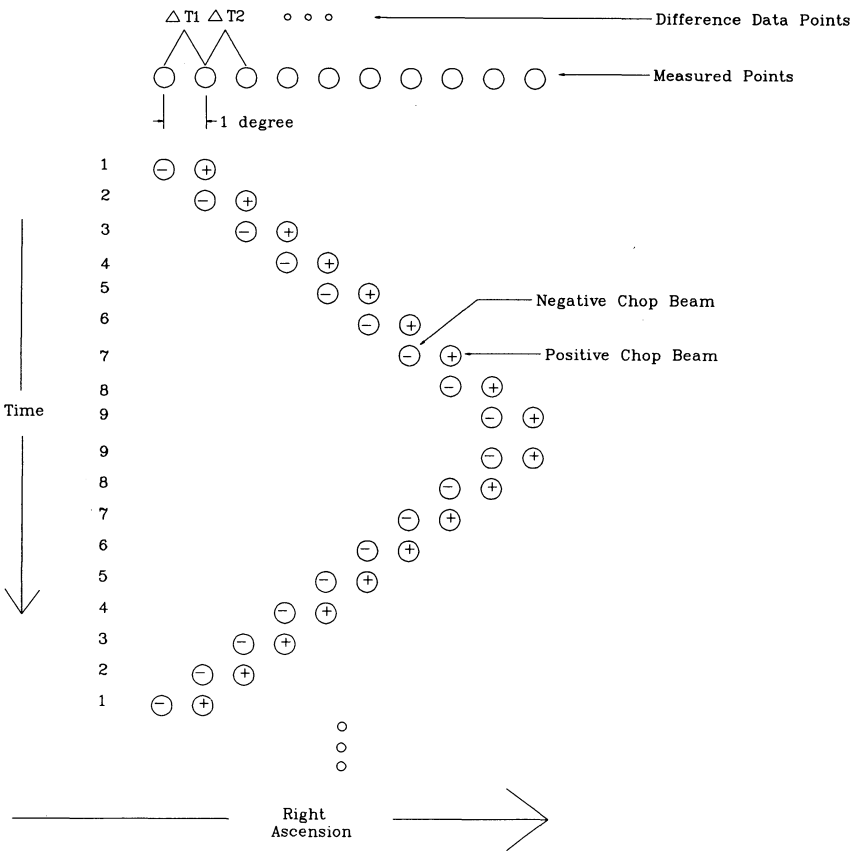

FIG. 18.—CBR scanning strategy. Ten fields were measured from nine telescope positions. One minute integrations were performed at each azimuth position before stepping to the next azimuth position.

total integration time per point constant. This provided an efficiency of ~65%. The servo was not completely optimized at the time, and was improved for the 1990–1991 polar expedition.

At 90 GHz, the principle Galactic foreground contaminant is dust. Using the *IRAS* 100 μm map, a region of the sky with low dust emission was chosen, centered at $\alpha = 21.5$ hr, $\delta = -73°$. Based on the balloon measurement of dust in the Galactic plane, this region has a total dust emission at 90 GHz of 50–100 μK, with first differences of 20–30 μK. The region was also far from the position of the Sun during the data taking period. Given the low level of dust contamination expected, and some uncertainty in the absolute elevation, no dust subtraction was performed. As the final conclusions from the data are stated in terms of an upper limit, this should not cause any significant error. With the factor of two improvement in the newest data (Devlin et al. 1992; Meinhold et al. 1992) galactic dust has had to be carefully considered.

As stated above, the system was operational by the second week of December. The science data were taken between December 18 and January 3. Most of the integration time was spent on a strip of nine points centered at $\alpha = 21.5$ hr, $\delta = -73°$. A significant amount of data was obtained on an overlapping nine-point strip centered at $\alpha = 22.47$ hr, $\delta = -73°$, and on the two strips 0.5 degrees above and below $\delta = -73°$, again centered on $\alpha = 21.5$. In addition, measurements of sky noise were done with the telescope azimuth fixed.

5.4. *Weather and Atmospheric Contributions*

The sky at the South Pole varied from dark blue to a dark gray, caused by "ice clouds." Several times there was a light snow, usually attributed to blown particles rather than to precipitation. These rare occasions required dusting off the primary mirror (although the light layer of ice crystals was not obvious in the data). The sky temperature at the measurement elevation (10 K + 3 K for the CBR), added to the system temperature (about 40 K), gives a theoretical chopped rms noise of 4.6 mK $s^{1/2}$ (antenna temperature). The observed noise was ~6.1 mK $s^{1/2}$, which may have been due to short-term sky variations. The condition of the sky could generally be ascertained by observing the realtime data stream from the telescope; for particularly bad days, random variations in the offset of many tens of milliKelvin over several second time scales would occur, while for the clearest sky, no structure could be seen over the noise level of ~6.1 mK rms (the sampling and lockin integration is ~1 s). This noise level also varied slightly, noise as low as 5 mK $s^{1/2}$ and as high as 8 mK $s^{1/2}$ were not uncommon on "good" days.

The atmosphere on good days at the South Pole was extraordinarily stable at 90 GHz, where the emission is dominated by oxygen and water. Figure 19 is an FFT of the differential temperature data taken with the telescope position fixed. What is evident from the plot is that the 1/f knee of the combination of the system and the sky is at ~2000 seconds,

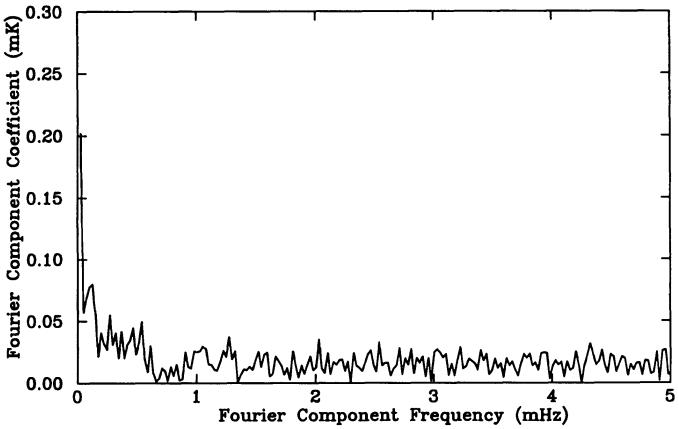

FIG. 19.—Fast Fourier Transform of fixed azimuth data from the South Pole on 1988 December 27. The 1/f knee is at ~2000 s.

extremely long for this type of measurement. There are two interesting results of this stability. The first is that the data should integrate down very well, which is true. The second shows up in data from the full scans: the high stability of the atmosphere shows up in the persistence of large-scale structures. In other words, since bulk motions seem to be happening slower than a few thousand seconds, scans over a large angle in less than 1000 s measure the contours of any pressure or temperature gradients which are there. For an order of magnitude estimate, consider that the ambient pressure at the South Pole is ~500 mb, and that there are random pressure variations of order 1%, or 5 mb per day. Given a zenith sky temperature of 9 K, or 7 K from oxygen, there will be temperature differences of order 70 mK on large angular scales when looking toward regions of high pressure versus regions of lower pressure. There are complications about the size and shape of the atmospheric perturbations associated with the high and low pressures, as well as the effect of looking toward these regions at an angle of 73° from the horizon, but the basic effect can be large. Large-scale atmospheric perturbations may be a significant effect in the data as illustrated in Figure 20. This shows two small subsets of the data, including only one full scan each. Large gradients are apparent in both data sets, and these gradients differ significantly from one another. The data displayed have unusually large gradients compared to most of the data set, but are well within the data editing requirements stated below. If these gradients are due to the atmospheric phenomena discussed above, then they might average to zero after enough scans. In fact, most of the signal does average away upon summing the data set, but there is a residual gradient (see Fig. 21). Whether this is due to intrinsic CBR structure, statistical fluctuations in the atmospheric gradients discussed below, or some more complex phenomena like the Sun-synchronous atmospheric tides or internal systematic errors is unknown. The gradients must be removed and the upper limits calculated taking this fit into account. This type of pressure-driven atmospheric effect is a potential problem for all ground-based measurements of this kind and might be expected to be more severe on larger angular scales.

5.5. *Data Manipulation and Statistics*

Bad weather data were removed by removing sections where either the 100 s rms was more than three times normal, or where the 100 s average was more than 10 σ different from the previous average. For "good" days, the procedure removes little data, and there are very long stretches where no data at all are removed. The nutation system had intermittent periods of erratic behavior, so a cut similar to that described above was applied using the amplitude of the nutation. In addition to variations induced by large atmospheric variations, the editing procedure removes data contaminated by some of the high power radio communications used at the South Pole station. Possible RF contaminants were investigated; only one which caused a severe problem, occurring a few minutes before an airplane landed, was found. This is probably due to the L-band transponders carried by the C-130 Hercules airplanes, and activated by the Pole station ground control. The effects are thus limited to a short time and are easily distinguishable. Weather records, plane schedules, and communication times were logged.

Deep CBR integrations were made at $\delta = -73°$, centered at $\alpha = 21.5$ hr (referred to as region 1) and 22.47 hr (region 2) between December 20 and 30. Resulting in a total of 95 hr data after editing, and with a total time spent on the points of interest of 44 hr on region 1 and 13 hr on region 2. Measurements at $\delta = -73°.5$ and $-72°.5$ were essentially lost to weather and nutation mechanism problems.

Generally in an experiment of this type, there will be slow

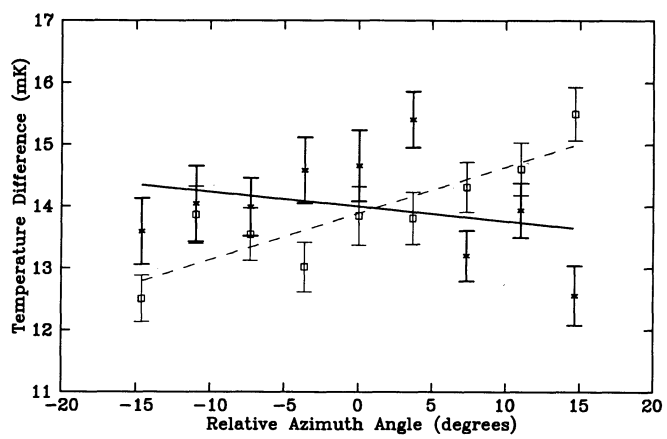

FIG. 20.—Summed data from two short sections, each including at least one full scan in azimuth. This shows evidence for changing linear drifts. No fitting has been done to either of these data sets.

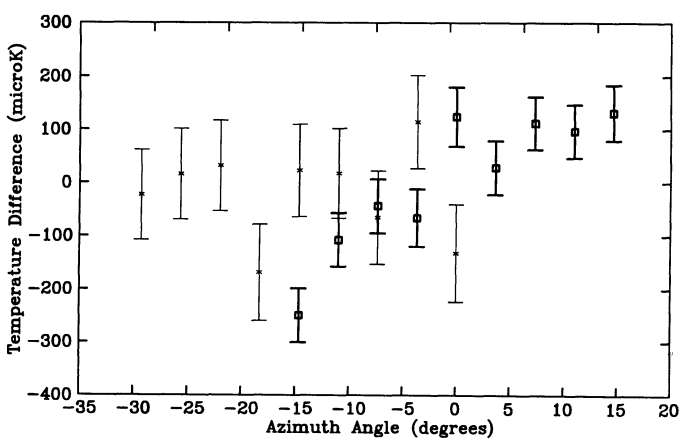

FIG. 21.—Summed data from region 1 (*boxes*) and region 2 (*asterisks*). The data has had a linear fit in *time* removed from each *full* scan before binning in azimuth.

changes in the offset which may be due to atmospheric effects similar to those described above, or small, changing temperature gradients on the primary or baffles, electronic offsets and so on. These slowly changing offsets should be removed in such a way as to avoid removing real structure in the data or adding false signals. Since the fields were scanned first in one direction and then back the other way, variations over the time to complete one scan in each direction (referred to as a full scan) can be removed without removing any intrinsic structure. Figure 21 is the data from the two regions measured around $\alpha = 21.5$, $\delta = -73°$, binned in angle after removing linear fits in time over full scans. The errors are shown as measured statistical $\pm 1\ \sigma$ error bars. The overlapping regions help to test for gross sidelobe effects or other significant systematic trends which might be in the data. As there is no obvious correlated structure between the data sets, and as the scatter in each is close to what one might expect from random data it would appear that there are no large systematic errors dependent upon scan angle relative to the Sun (for instance).

The fact that the slopes of the two data sets shown in Figure 21 are different shows that these linear components are not intrinsic to the CBR. Some improvement in overall noise can be obtained while removing the spurious linear component by removing linear trends in angle from individual "half scans," since this should remove most of the time drifts and the scatter associated with the changing linear angle components. Figure 22 shows the results of fitting the raw data for region 1 to first order in angle over half scans, then binning.

As an added test of the statistics, a histogram of the values going into each bin was calculated. Figure 23 is the distribution of the data in one bin after the fitting procedure described above, including all 14,800 1 s data points, along with the best-fit Gaussian. The dispersion of the Gaussian is 6.1 mK, which corresponds to the final error bar of 50–55 μm K per azimuth bin. Of course this plot does not show directly that the errors are uncorrelated, but the result is at least consistent with that interpretation.

6. FURTHER MEASUREMENTS

The stabilized platform ballooning program has been continued since returning from the South Pole. In 1989 November, the telescope was flown with a four-channel, 300 mK, helium-3 bolometer detector in place of the SIS detector, as part of the NSF Center for Particle Astrophysics (CfPA) program, in collaboration with the Richards and Lange groups at UC Berkeley. In this configuration the experiment is called the Millimeter Anisotropy eXperiment (MAX). The platform flew from the NASA NSBF facility in Fort Sumner, New Mexico, and obtained 10 hr at float altitude. The pointing system operated without significant problems, as did the detectors.

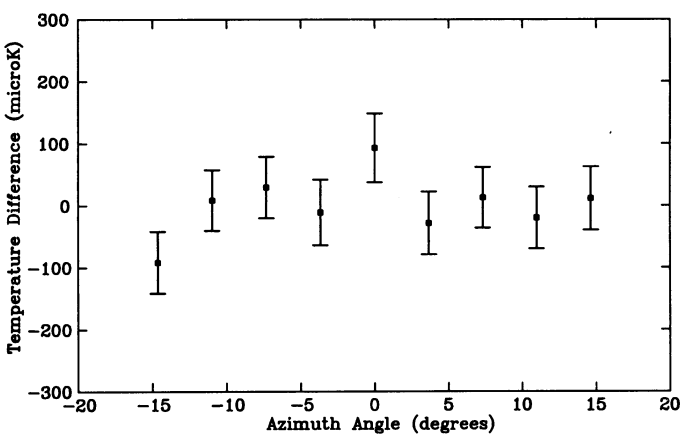

FIG. 22.—Summed data from region 1. The data has had a linear fit in *angle* removed from each *half* scan before binning in azimuth.

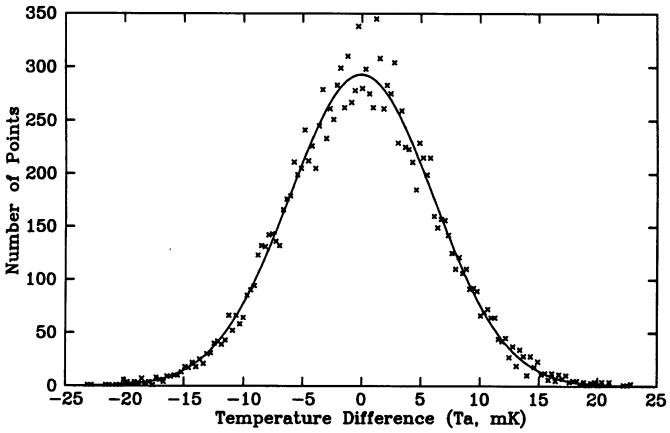

FIG. 23.—Distribution of data in bin 6 (*symbols*) with the best-fit Gaussian (*solid line*). This data includes linear fits over half scans in azimuth. The best-fit Gaussian has $\sigma = 6.1$ mK T_{antenna}. The total number of points was 14,800.

This detector system, in a three-frequency configuration, has been flown two more times, once in 1990 July and once in 1991 June, both from the NSBF facility in Palestine, Texas. Details of this instrument, as well as data from the flights and discussion of systematic effects can be found in Fischer et al. (1992), Alsop et al. (1992), Devlin et al. (1992), and Meinhold et al. (1992). A similar detector cooled to 100 mK by an Adiabatic Demagnetization Refrigerator (ADR) is also being developed at UC Berkeley and will be flown on the gondola soon. Flights using arrays of these detectors are planned for the future.

In addition to the balloon program, the South Pole measurements have been continued, with an expedition from 1990 November through 1991 January. Two separate detectors were employed during this expedition: the original SIS system discussed in this article and a new direct-amplification HEMT-based receiver, operating over a 10 GHz bandwidth centered at 30 GHz. This system has an effective FWHM of $\sim 1.^{\circ}5$ and a sensitivity below 1 mK $s^{1/2}$. Data from this expedition will be discussed in an upcoming paper (Gaier et al. 1992).

7. CONCLUSION

We have constructed and flown a stabilized platform and high performance off axis telescope system for making anisotropy measurements of the CBR at millimeter wavelengths, on angular scales of 5′ to a few degrees. The first flight of the system showed substantially higher emission at 3.3 mm from galactic dust than expected from the standard models. Measurements of CBR anisotropy have been made from both balloons and the South Pole, and 95% confidence level upper limits of 96 μK, or $\Delta T/T < 3.5 \times 10^{-5}$ for Gaussian autocorrelation functions have been set. A factor of 10 increase in sensitivity is a realistic possibility within the next few years with new detector technologies.

The flexibility of the design of the instrument and the relevance of the angular scale studied have been proven, and the

instrument will be used to make even more sensitive measurements using improved detectors. With currently planned instruments, we hope to make small maps at a level of $\Delta T/T$ = few times 10^{-6}, obtaining spatial information on any structures which might be found.

This work was supported by the National Aeronautics and Space Administration, under grant NAGW-1062 and GSRP grant NGT-50192, the National Science Foundation Polar grant DPP878-15985, California Space Institute grant CS 35-85, the University of California, and the US Army. T.V. acknowledges the financial support of CNPq under grant 910231/87-7-FA, through the CNPq/NSF cooperation program, and from the Brazilian Antarctic program under grant PROANTAR 9630. We also gratefully acknowledge the support of the NSF Center for Particle Astrophysics. We particularly want to thank Nancy Boggess for her vision of the viability of this research and for her continued support. This work would not have been possible without the support and encouragement of Richard Muller, Fred Gillett, Buford Price, and John Lynch. We wish to thank Anthony Kerr and S. K. Pan of NRAO for supplying the exceptional SIS mixer. The Nb/Al-Al_2O_3/Nb junctions used were supplied by Hypres corporation. Special thanks to Joe Stack and Paul Moyer at Bell Labs for machining the primary and secondary mirrors. Robert Wilson, Anthony Stark, and Corrado Dragone, all of AT&T Bell Laboratories provided critical support and discussion regarding the early design of the telescope and receiver system. We would like to thank Bill Coughran and all of the South Pole support staff for highly successful 1988–1989 and 1990–1991 polar summers. In addition, we want to acknowledge the crucial contributions of the entire team of the National Scientific Balloon Facility in Palestine Texas for their continued excellent support.

REFERENCES

Alsop, D. C., et al. 1992, 395, 317
Bond, J. R., & Efstathiou, G. 1987, MNRAS, 226, 655
Bond, J. R., Efstathiou, G., Lubin, P. M., & Meinhold, P. R. 1991, Phys. Rev. Lett., 66, 2179.
Bouchet, F. R., Bennett, D. P., & Stebbins, A. 1988, Nature, 335, 410
Chingcuanco, A. O. 1989, Ph.D. thesis, University of California at Berkeley
Chingcuanco, A., Lubin, P., Meinhold, P., & Tomizuka, M. 1990, ASME J. Dyn. Syst., Meas., Control, 112, 703
Conklin, E. K. 1969, Nature, 222, 971
Corey, B. E., & Wilkinson, D. T. 1976, BAAS, 8, 351
Cottingham, D. 1990, paper presented at Aspen Winter Conf. on Astrophysics: The Cosmic Background Radiation, Aspen, Colorado
Davies, R. D., Lasenby, A. N., Watson, R. A., Daintree, E. J., Hopkins, J., Beckman, J., Sanches-Almeida, J., & Rebolo, R. 1987, Nature, 26, 462
Devlin, M., et al. 1992, in Proc. NAS Colloq. on Physical Cosmology (Irvine, CA), in press
Dragone, C., & Ruscio, J. T. 1985, AT&T Bell Labs. Tech. Mem. WPN: 311301-0399, File Case: 20564
Dragovan, M. 1987, paper presented at UC Santa Barbara Colloq.
Fischer, M. L., et al. 1992, ApJ, 388, 242
Fixsen, D. J., Cheng, E. S., & Wilkinson, D. T. 1983, Phys. Rev. Lett., 50, 620
Gaier, T., Schuster, J., Gundersen, J., Koch, T., Seiffert, M., Meinhold, P., & Lubin, P. 1992, ApJ, 398, L1
Lubin, P. M., Epstein, G. L., & Smoot, G. F. 1983a, Phys. Rev. Lett., 50, 616
Lubin, P. M., & Villela, T. 1986, NATO Conf. Proc. Galaxy Distances and Deviations from Universal Expansion, ed. B. F. Madore & R. B. Tully (Dordrecht: Reidel), 169
Melchiorri, F., Melchiorri, B. O., Ceccarelli, C., & Pietranera, L. 1981, ApJ, 250, L1
Meinhold, P. R., & Lubin, P. M. 1991, ApJ, 370, 11
Meinhold, P., et al. 1993, in preparation
Meyer, S. S., Page, L., & Cheng, E. S. 1991, ApJ, 371, L1
Pan, S. K., Kerr, A. R., Feldman, M. J., Kleinsasser, A. W., Stasiak, J. W., Sandstrom, R. L., & Gallagher, W. J. 1989, IEEE Trans. Microwave Theory Tech., 37, 3
Rees, M. J., & Sciama, D. W., 1968, Nature, 217, 511
Readhead, A. C. S., Lawrence, C. R., Myers, S. T., Sargent, W. L. W., Hardebeck, H. E., & Moffet, A. T. 1989, ApJ, 346, 566
Sachs, R., & Wolfe, A. 1967, ApJ, 147, 73
Silk, J., 1984, in Proc. Plasma Astrophysics: International School and Workshop in Astrophysics, ed. T. D. Guyenne & J. J. Hunt (Varenna) (Noordwijk: ESTEC)
Smoot, G. F., Gorenstein, M. V., & Muller, R. A. 1977, Phys. Rev. Lett., 39, 898
Smoot, G. F. et al. 1992, ApJ, 396, L1
Strukov, I. A., & Skulachev, D. P. 1984, Soviet Astron. Lett., 10, 1
Sunyaev, R. A., & Zel'dovich, Ya. B. 1972, Comment. Astrophys. Space Sci., 4, 173.
Thomas, B. M. 1978, IEEE Trans. Antennas Propag., AP-26(2), 367
Vittorio, N., Matarrese, S., & Luccin, F. 1988, ApJ, 328, 69
Vittorio, N., Meinhold, P. R., Muciaccia, P. F., Lubin, P. M., & Silk, J. 1991, ApJ, 372, 1
Wright, E. L. 1992, ApJ, 396, L13